Resolving chiral transitions in one-dimensional Rydberg arrays with quantum Kibble-Zurek mechanism and finite-time scaling

Soto Garcia, Jose; Chepiga, Natalia

DOI
10.1103/PhysRevB.110.125113

Publication date
2024

Document Version
Final published version

Published in
Physical Review B

Resolving chiral transitions in one-dimensional Rydberg arrays with quantum Kibble-Zurek mechanism and finite-time scaling

Jose Soto Garcia and Natalia Chepiga
Kavli Institute of Nanoscience, Delft University of Technology, Lorentzweg 1, 2628 CJ Delft, The Netherlands

(Received 11 March 2024; revised 25 July 2024; accepted 22 August 2024; published 9 September 2024)

The experimental realization of the quantum Kibble-Zurek mechanism in arrays of trapped Rydberg atoms has brought the problem of commensurate-incommensurate transition back into the focus of active research. Relying on equilibrium simulations of finite intervals, direct chiral transitions at the boundary of the period-3 and period-4 phases have been predicted. Here, we study how these chiral transitions can be diagnosed experimentally with critical dynamics. We demonstrate that chiral transitions can be distinguished from the floating phases by comparing Kibble-Zurek dynamics on arrays with different numbers of atoms. Furthermore, by sweeping in the opposite direction and keeping track of the order parameter, we identify the location of conformal points. Finally, combining forward and backward sweeps, we extract all critical exponents characterizing the transition.

DOI: 10.1103/PhysRevB.110.125113

I. INTRODUCTION

Understanding the nature of quantum phase transitions (QPTs) in strongly correlated low-dimensional systems is one of the biggest challenges in modern condensed matter physics [1,2]. The development of conformal field theory (CFT) [3,4] has led to the discovery of many fascinating critical phenomena with dynamical critical exponent $z = 1$. The latter implies, in particular, a quantum-classical correspondence, which opens a way to study QPT with models of classical statistical mechanics.

The construction of advanced entanglement-based numerical techniques such as tensor network algorithms [5–8] and recent progress in quantum simulating platforms have further stimulated the discovery of exotic critical phenomena, putting a focus onto quantum versions of phase transitions. The study of phase transitions beyond CFT, although extremely challenging, has been attracting a lot of attention in the past decades. One of the most intriguing and debated problem is a possibility of a direct chiral transition out of crystalline period-3 phase predicted by Huse and Fisher [9] in the context of adsorbed monolayers [10–14].

Recent experiments on Rydberg atoms have shed new light onto this originally classical problem, but now in the context of one-dimensional (1D) quantum chains [15–24]. In these experiments, Rydberg atoms are trapped with optical tweezers at a well-controlled inter-atomic distance. Competition between the laser detuning, favoring atoms to be in Rydberg states, and strong van der Waals repulsions between them leads to a rich phase diagram dominated by lobes with integer periodicities $p = 2, 3, 4, \ldots$

Although quantum-classical correspondence does not hold for nonconformal criticality, many features of the transitions with $z \neq 1$ are qualitatively similar [9,17,18,20,25]. In particular, using Huse and Fisher's original criteria for chiral transitions and numerical simulations with state-of-the-art density matrix renormalization group algorithm [5–7], it has been shown that in Rydberg arrays, the transition out of $p = 3$ phase changes its nature multiple times [17–19,26]. At the point where chiral perturbations vanish, the transition is conformal in the three-state Potts universality class; away from this point but not too far from it the transition is direct in the Huse-Fisher universality class; further away the transition is a two-step process via conformal Kosterlitz-Thouless [27] and nonconformal Pokrovsky-Talapov [28] transitions, with a floating phase between the two. Quite surprisingly, numerical simulations revealed that the boundary of the $p = 4$ phase undergoes a similar zoo of QPTs with a conformal Ashkin-Teller point, followed by the $p = 4$ chiral transition, and then by the floating phase [18,20].

Intervals of chiral transitions predicted numerically explain the experimental data obtained with Rydberg atoms. However, the numerical methods used to diagnose phase transitions differ greatly from the experimental techniques. Numerical simulations mainly rely on equilibrium physics and extracted critical exponents ν of the correlation length, $\tilde{\beta}$ of the incommensurate wave vector, and α of the specific heat. At the same time, the experiments are performed out of equilibrium, employing quantum Kibble-Zurek (KZ) mechanism [15,29,30], which tracks the number of domain walls (kinks) formed upon sweeping through a phase transition as a function of sweep rate. This paper aims to fill the gap between the theoretical predictions for chiral transitions and experimentally accessible measurements to diagnose them.

II. KIBBLE-ZUREK MECHANISM

The KZ mechanism describes the generation of topological defects during the constant-rate drive of a system through a second-order phase transition [31]. The concept, introduced by Kibble to explain galaxy formation in the nascent universe [32], was brought to condensed matter by Zurek [33] and recently has been extended to QPTs [29,30,34]. In the critical region, the correlation length $\xi \sim |g - g_c|^{-\nu}$ and the

relaxation time $\tau \sim |g - g_c|^{-\nu z}$ diverge with the distance to the transition $|g - g_c|$. Sweeping through the transition in a nonadiabatic fashion with a given sweep rate s creates a certain density of kinks (domain walls) n_k, that, in turn, determines the final correlation length $\hat{\xi}$ measured deep in the ordered phase. According to the KZ mechanism, the scaling of both quantities is universal and governed by the critical exponent $\mu = \nu/(1 + \nu z)$:

$$n_k \sim \hat{\xi}^{-1} \sim s^{-\mu}. \tag{1}$$

III. FINITE-TIME SCALING

Finite-time scaling (FTS) is the temporal analog of the finite-size scaling performed in the critical region when the system size L used in numerical (or quantum) simulations is smaller than the actual correlation length. FTS allows accessing the scaling of macroscopic quantities in the nonadiabatic region. For Rydberg arrays, such analysis has been performed only for the correlation length [15].

Inspired by the results for the chiral clock model [35], we perform FTS by sweeping from the ordered to the disordered phase—in the direction opposite to the conventional Kibble-Zurek drive. If the KZ mechanism tracks the formation of domain walls in the ordered phase, then the backward sweeping captures the inertia of the order parameter—the faster one sweeps through the transitions, the deeper in the disordered phase is the point g_0 where the order parameter vanishes [36–38]:

$$|g_0(s) - g_c| \propto s^{\frac{\mu}{\nu}}. \tag{2}$$

At the critical point, the remaining order parameter O_c scales with the sweep rate as [36–38]

$$O_c(s) \propto s^{\beta \frac{\mu}{\nu}}. \tag{3}$$

These complete the set of independent critical exponents, allowing to extract μ, ν, β, and z and derive other critical exponents using the hyperscaling relation $2 - \alpha = \nu(1 + z)$.

IV. BLOCKADE MODEL

An array of Rydberg atoms can be described by the Hamiltonian of interacting hard-core bosons:

$$H = \frac{\Omega}{2} \sum_i \left(d_i + d_i^\dagger\right) - \Delta \sum_i n_i + \sum_{i<j} V_{ij} n_i n_j, \tag{4}$$

where Ω is the Rabi frequency bringing an atom to the Rydberg state, Δ is laser detuning, and $V_{ij} \propto 1/r^6$ is a van der Waals interaction.

Owing to an extremely strong repulsion at short distances, we can write down an effective Hamiltonian with r-site blockade:

$$H = \sum_i -\frac{\Omega}{2}(d_i^\dagger + d_i) - \Delta n_i + V_{r+1} n_i n_{i+r+1} \tag{5a}$$

$$n_i(n_i - 1) = n_i n_{i+1} = \cdots = n_i n_{i+r} = 0. \tag{5b}$$

All operators in Eq. (5a) are acting in the constrained Hilbert space defined by Eq. (5b), which implies that two atoms cannot be excited within a certain distance r. The next-to-blockade interaction is encoded in the third term and the rest of the decaying interaction tail is set to zero. Various blockade ranges give access to different slices of the phase diagram [20]: we will use $r = 1$ blockade to probe chiral transition out of period-3 phase and $r = 2$ for the period-4 case. The advantage of the blockade model is three-fold: (i) it provides a good approximation to the van der Waals potential [17,18,20]; (ii) tensor networks with explicitly implemented blockade have significantly lower computational costs [16,20]; (iii) for these models, the location and extent of chiral transitions are known with a high accuracy [17,20].

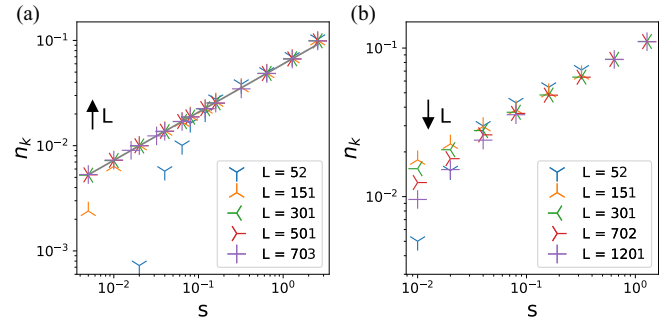

FIG. 1. Scaling of the density of kinks n_k with the sweep rate s through (a) the direct transition and (b) the floating phase. Arrows show systematic finite-size effects that can be used to resolve the two critical regimes. The gray line is a linear fit in a log-log scale.

Numerical simulations were performed with the time-evolving block decimation algorithm (TEBD) with time step $\delta t = 0.1$ and maximal bond dimension $D = 400$ (see Appendix A for further technical details).

V. FLOATING PHASE VERSUS DIRECT TRANSITION

Our first goal is to resolve the direct chiral transition from the intermediate critical phase. Upon approaching the floating phase from the disordered one, the correlation length ξ diverges stretch-exponentially due to Kosterlitz-Thouless transition [27], leading to the effective exponent $\nu_{\text{eff}} \to \infty$, and consequently $\mu_{\text{eff}} \to 1$. Interestingly, this value is much larger than the one for the three-state Potts ($\mu = 5/11$) or Ashkin-Teller ($0.4 \leqslant \mu \leqslant 0.5$) transitions. But we rely on the fact that this scaling is only approached asymptotically and otherwise is affected by significant finite-size effects [39,40].

In Fig. 1(a), we present the scaling of the density of kinks formed by sweeping through the direct transitions for various system sizes. For a given size L, there is a certain range of sweep rates s where the scaling in log - log plot is linear, in agreement with KZ mechanism. However, the curves turn down for small s, where the system dynamics approaches the adiabatic regime for a given L. This is similar to when one underestimates a correlation length when it is comparable to or exceeds the chain length. The window of the universal KZ scaling can be increased by increasing the length L. In other words, comparing the density of kinks at low sweep rates for several system sizes, we see that it grows with L.

Across the floating phase, the finite-size effect is very different, as presented in Fig. 1(b): The larger the system size, the closer to the asymptotic limit, and therefore the steeper the scaling is. Focusing again on low sweep rates, we see a

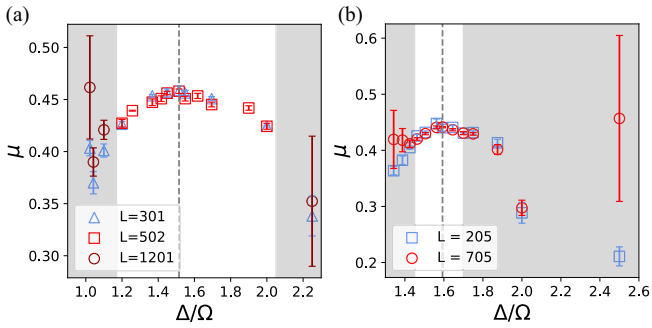

FIG. 2. Critical exponent μ extracted with the Kibble-Zurek mechanism along various cuts through the transitions (a) into the period-3 phase with $r = 1$ blockade and (b) into the period-4 phase with $r = 2$ blockade. The vertical dashed line indicates the location of the conformal point. The shaded region states for the floating phase. In this area, the Kibble-Zurek mechanism is not defined, and our results should be taken only as μ_{eff}. At the conformal points (dashed lines), the extracted values of μ agree with theory predictions within 1%. Error bars reflect errors from the fit but do not show errors due to entanglement cutoff.

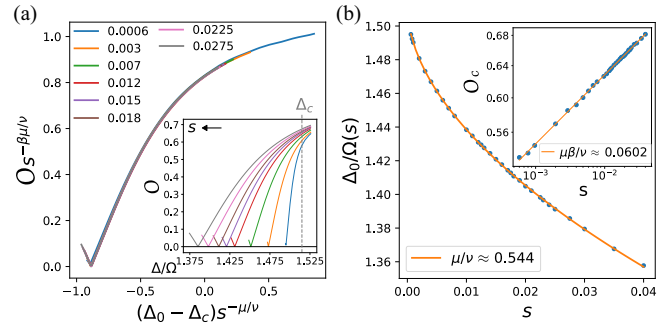

FIG. 3. Example of the finite-time scaling out of period-3 phase. (a) Order parameter as a function of the sweep rate after the re-scaling indicated at each axis. The inset shows the same curves before the re-scaling. (b) Location of the point Δ_0, where the order parameter vanishes as a function of sweep rate. Inset: Scaling of the order parameter O at the critical point Δ_c as a function of sweep rate s. Orange lines are fits with Eqs. (2) and (3).

systematic and fast decrease in kinks density with L. However, the limitation of measurable density of kinks for very small system size L is still in place, as can be clearly seen for $L = 52$.

To summarize, for a set of sufficiently large system sizes, the density of kinks grows with the system size towards the universal KZ scaling when the system is driven through a direct transition and n_k decays significantly when sweeping through the floating phase.

VI. CONFORMAL VERSUS CHIRAL TRANSITIONS WITH KZ MECHANISM

We have defined a protocol to distinguish the direct transition from the floating phase. Now let us see if with critical dynamics we could identify when the transition is conformal. For this purpose, we systematically extract the KZ critical exponent μ across various cuts into period-3 and period-4 phases. Our numerical results are summarized in Fig. 2. For the model with $r = 1$ blockade, there is only one conformal critical point, and its location is known exactly [26]. For the model with $r = 2$ blockade, the location of the conformal point has been obtained numerically by tracking the commensurate line where chiral perturbations vanish [20].

For both transitions into period-3 and period-4 phases, the KZ critical exponent μ measured for a set of consecutive cuts has a dome shape, taking maximal values at the cuts that go through the conformal points. Numerically obtained values $\mu \approx 0.458$ for the three-state Potts and $\mu \approx 0.442$ for the Ashkin-Teller point (with $\nu \approx 0.78$ [20]) agree within 1% with the CFT predictions. Away from conformal points, μ shows a slow decay. The domelike shape we observe here is in excellent agreement with the experimental results [15], and has been overlooked in the previous numerical simulations of dynamics hidden by large numerical errors [15].

By looking at Fig. 2 with marked conformal points, it is easy to associate them with maxima of μ. However, if the location of these points were unknown (as is often the case in experiments), then the problem would be quite challenging since the domes are relatively flat. As a solution, we propose performing a backward sweep.

VII. SWEEPING FROM THE ORDERED TO THE DISORDERED PHASE

Sweeping from the ordered to the disordered phase—in the direction opposite to the KZ mechanism—allows us to study a relaxation of the order. The faster is the sweeping rate the longer it takes for the order parameter to disappear after crossing the transition, as illustrated by the inset of Fig. 3(a). We extract the ratio μ/ν by fitting the location where the order parameter vanishes with Eq. (2), as shown in Fig. 3(b). Furthermore, we extract $\beta\mu/\nu$ in the inset by fitting the order parameter at the critical point with Eq. (3).

Combining the results from the two fits, we extract the critical exponent β along various cuts from period-3 and period-4 phases. The results are summarized in Figs. 4(a) and 4(b) correspondingly. Similar to the Kibble-Zurek critical exponent μ, we find that β takes its maximal values at

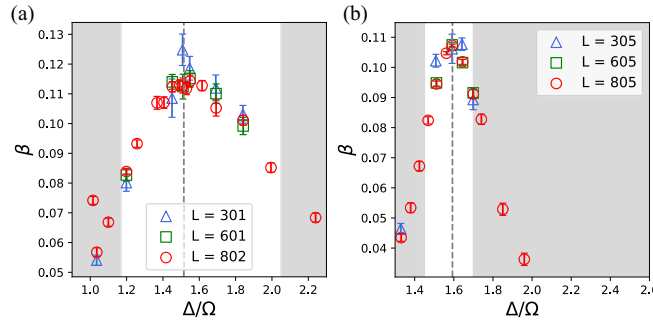

FIG. 4. Critical exponent β measured with finite-time scaling of the order parameter while sweeping from the ordered (a) period-3 and (b) period-4 phases to the disordered one. In both cases, the conformal points (dashed lines) correspond to the pronounced peaks in β. Shaded regions indicate the floating phases.

the conformal points. However, the sharp peaks in β allow identifying the location of the critical point with significantly smaller uncertainty.

It is important to keep in mind that the critical exponent β is well understood only for the two conformal points. At the three-state Potts point, it takes the universal value $\beta = 1/9$. Our numerical result $\beta \approx 0.112$ agrees within $\sim$2% with this value. As long as the transition to the disordered phase is direct and the order parameter goes to zero at the transition, the exponent β can be formally defined. However, its value is unknown and might be affected by the domain wall tension [9]. Indeed, what we observe is that β is not universal and varies along the chiral transition, decaying away from the conformal point. This fully agrees with previous numerical results on the chiral clock model where the exponent β for chiral transitions has been extracted [35].

Ashkin-Teller critical theory defines the family of universality classes with the exponents $\frac{1}{12} \leqslant \beta \leqslant \frac{1}{8}$ and $\frac{2}{3} \leqslant \nu \leqslant 1$ satisfying $d = \beta/\nu = 1/8$ [41]. Our numerical result $\beta \approx 0.1073$ belongs to the corresponding interval. Equilibrium simulations have reported an Ashkin-Teller point with $\nu \approx 0.78$ [20], implying $\beta \approx 0.098$. This value agrees with our out-of-equilibrium result within 10%. Similar to the period-3 case, we see that the value of β is not universal along the $p = 4$ chiral transition.

VIII. COMBINATION OF FORWARD AND BACKWARDS SWEEPING

Combination of forward and backwards sweeping opens a way to extract all critical exponents, including the dynamical critical exponent z presented in Figs. 5(a) and 5(c): at the two conformal points our numerical results match the CFT value $z = 1$; away from these points z increases, in agreement with previous studies [15,20]. We also extract the critical exponent α. Unlike other critical exponents, α does not change significantly along the chiral transitions. This agrees with the idea that along chiral transitions, α keeps the value it takes at the conformal point [42–44].

IX. RESULTS FOR THE RYDBERG MODEL WITH $1/r^6$ INTERACTION

We have verified whether our results on the blockade model can be extrapolated to the Rydberg model with the $1/r^6$ van der Waals interaction.

By sweeping from the disordered to the period-3 phase we extract the critical exponent μ for various cuts along the transition. The results are summarized in Fig. 6(a). The point where the critical exponent μ takes the maximal value is in good agreement with previously identified location of the three-state Potts point. Interestingly, above the Potts point, μ decays very slowly, in agreement with an extended interval of the chiral transition. However, although the qualitative shape of Fig. 6(a) is similar to the one of Fig. 2(a), the values of μ seem to be above the theoretical ones, with a discrepancy of 5% for μ on the Potts point respect to the CFT prediction $\mu \approx 0.454$.

We believe, this discrepancy is due to the small system sizes and fast sweep rates used in the simulations due to numerical constraints. We expect that bigger system sizes and smaller sweep rates will allow a more accurate extraction of the critical exponents and to distinguish the floating phase from the chiral transition.

Sweeping on the opposite direction, from the period-3 to the disordered phase, we perform a finite-time scaling and

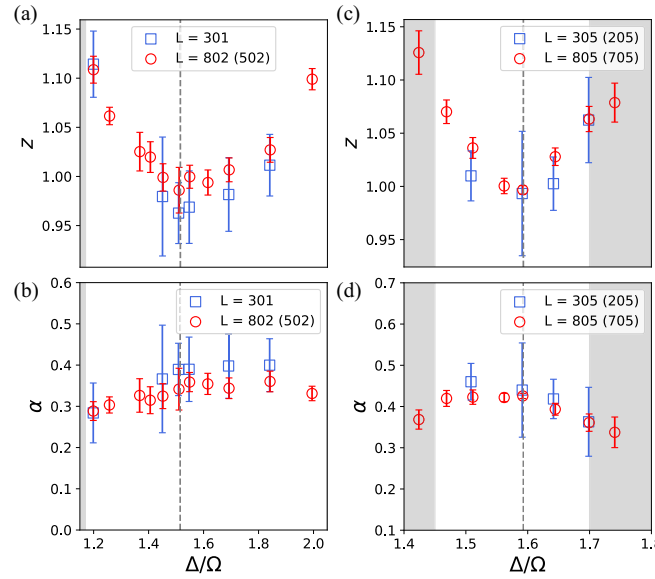

FIG. 5. Dynamical critical exponent z and specific heat critical exponent α computed across various cuts across transitions to the (a), (b) period-3 and (c), (d) period-4 phases. (a), (c) Our results agree with $z = 1$ at the two conformal points (dashed lines) and suggest that $z > 1$ when the transitions are chiral. (b), (d) Numerically extracted values of α are in good agreement with CFT predictions $\alpha = 1/3$ for three-state Potts and $\alpha \approx 0.44$ for the Ashkin-Teller point with $\nu \approx 0.78$. We show the results for small (blue) and large (red) system sizes; when L used in KZ and in finite-time scaling are different, the former is indicated in brackets. Shaded regions state for the floating phases.

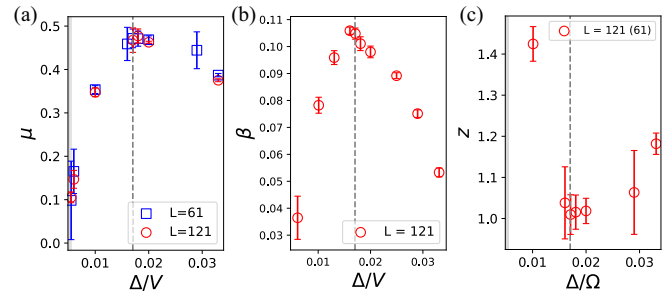

FIG. 6. Critical exponents (a) μ, (b) β, and (c) z computed across various cuts for the period-3 Rydberg model with $1/r^6$ interaction using KZ, FTS, and combining both techniques, respectively. When combining KZ with FTS, the system size for KZ is in brackets. Both μ and β have a dome shape that peaks at the conformal three-state Potts point. This peak is more pronounced for β, and agrees with theory prediction $\beta = 1/9$ for the three-state Potts point within 5%. z has a minimum $z \approx 1$ at the conformal point, which agrees with a conformal transition. Numerical results for μ agree within 5% with CFT predictions $\mu \approx 0.454$ for the three-state Potts point.

extract the critical exponent β by keeping track of the order parameter. Figure 6(b) depicts β for various cuts along the transition. Similar to the blockade model, we see a sharp peak in β around the conformal point. At the three-state Potts point, the extracted value of β agrees with the theory prediction $\beta = 1/9$ withing 5%.

Combining the results from KZ and FTS we extract the critical exponent z. Figure 6(c) shows z for various cuts along the transition. As it happened in the blockade model, z has a minimum at the conformal point and increases with the chiral perturbation. The calculated value of z in the predicted Potts point is $z = 1.01 \pm 0.05$, in agreement with a conformal transition.

X. DISCUSSION

In the present manuscript, we have shown how quantum phase transitions can be fully characterized by combining Kibble-Zurek dynamics with finite-time scaling of the order parameter. We demonstrated that the appearance of the intermediate floating phase can be identified by comparing Kibble-Zurek dynamics in Rydberg arrays with different numbers of atoms. Our approach relies on the standard Kibble-Zurek protocol and, by contrast to previous proposals, does not require measurements of the correlation length, incommensurate wave-vector [20] or structure factor [45] near or inside the critical region.

We have also shown that by sweeping from the ordered to disordered phase and keeping track of the order parameter, the location of the conformal points can be accurately identified with the critical exponent β. Although this method requires several runs terminating at different distances to the transitions, the ordered phases are less sensitive to noise, and the sampling might require only a few runs. To prepare a high-quality ordered state and to ensure an identical starting point for all samples, one can use a recently developed light-shift method [46]. Interestingly enough, when the location of the transitions is known, the KZ dynamics can be combined with measurements of the remaining order at the transition to extract the scaling dimension of the corresponding operator.

Our predictions for blockade models remain valid for the model Eq. (4) with van der Waals interaction. Performing a finite-time scaling of the period-3 order we observe a sharp peak in β that agrees with previously identified location of the conformal point [18]. At the same point, the KZ exponent μ takes its maximum. The interval of the $p = 4$ chiral transition in this model is very narrow [18], making it extremely challenging for dynamical studies. However, the protocols developed here are generic and can be applied to multicomponent systems, where the extent of the chiral transition can be controlled [47]. A similar qualitative effect of the chiral perturbation on the value of the critical exponents μ, β and ν has been previously reported in the chiral Potts [38] and chiral clock [48] models.

All these cases suggest that chiral transitions might form a weak universality class with critical exponents controlled by chiral perturbations. At the same time, when chiral perturbations become too strong, the chiral transitions are known to be unstable, and the floating phase opens. Taking a closer look to the critical exponent β presented in Fig. 4 we noticed that the value of this critical exponent at the point where the chiral transition terminates is roughly the same on both sides of the conformal points. Given the numerical errors in our data and the uncertainty in the location of the Lifshitz points, we cannot exclude a simple coincidence. However, the possibility that chiral transition terminates once beta drops to a certain universal value deserves a detailed and systematic investigation. We hope that our results will stimulate further theoretical exploration of the universal properties of these exotic transitions.

ACKNOWLEDGMENTS

N.C. acknowledges useful discussions with H. Bernien, F. Mila, and R.-Z. Huang. This research has been supported by Delft Technology Fellowship. Numerical simulations have been performed at the DelftBlue HPC and at the Dutch national e-infrastructure with the support of the SURF Cooperative.

APPENDIX A: BLOCKADE MODELS

1. Implementation details

This Appendix explains how Rydberg blockade can be encoded into one-dimensional (1D) tensor network. Note that various blockade ranges give access to different slices of the phase diagram, as explained in Ref. [20]. In this paper, we are focusing on transitions out of period-3 and period-4 phases. The tip of the period-3 phase, where the conformal three-state Potts critical point and two intervals of chiral transitions are realized, can be addressed with the $r = 1$ blockade model [17,18,26]. The tip of the period-4 phase, encompassing the Ashkin-Teller conformal point and two intervals of the $p = 4$ chiral transition, can be addressed with the $r = 2$ [20].

To fully profit from the reduced Hilbert space, a new basis was taken, wherein each element of the new basis is composed of a pair of adjacent local basis elements, where the last element of each tensor overlaps with the first site on the following tensor. In other words, we span the local physical degrees of freedom of each individual tensor over two consecutive atoms. Using the occupation of the atom shared between two nearest tensors as a quantum label of the auxiliary bond that connects them, we can bring the network into a block-diagonal form. The latter drastically reduces the computational complexity. Figure 7 illustrates how the $r = 1$ blockade basis is constructed.

The bulk Hamiltonian in the new $|h_i\rangle$ basis is

$$h_i = -\frac{\Omega}{2}(\tilde{a}_i\tilde{b}_{i+1} + \text{H.c.}) - \Delta\tilde{q}_i + V_2\tilde{q}_i\tilde{p}_{i+1}. \tag{A1}$$

The term $\tilde{a}_i\tilde{b}_{i+1} + \text{H.c.}$ represents the first term in Eq. (5a) of the main text. This term flips an atom between ground and Rydberg states. It comprises three local sites, with $\tilde{a}\,|h_1\rangle = |h_2\rangle$, and $\tilde{b}\,|h_1\rangle = |h_3\rangle$, and 0 otherwise. The operators $\tilde{q}_i$ and $\tilde{p}_i$ are local density operators for the left and right sites in each pair, returning nonzero values only for $\tilde{q}\,|h_3\rangle = |h_3\rangle$ and $\tilde{p}\,|h2\rangle = |h_2\rangle$ correspondingly. As a result, the next-nearest-neighbor interaction $V_2 n_i n_{i+2}$ transforms into a nearest-neighbor interaction $V_2\tilde{q}_i\tilde{p}_{i+1}$. To match the original

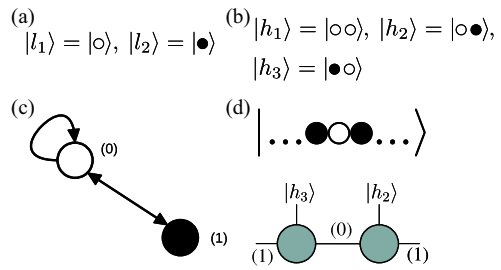

FIG. 7. Mapping of the $r = 1$ blockade model onto a model preserving the block diagonal structure of tensors. (a) Local Hilbert space $|l_i\rangle$ of the original model. (b) New local Hilbert space spanned over two consecutive sites. (c) Fusion graph for the recursive construction of the environment (both, left and right): starting with empty site (0), another empty site can always be added, ending up with label (0). Additionally, an occupied site can be added, leading to the label (1). On the other side, starting with label (1), only an empty site can be added, which results in label (0). (d) Example of the label assignment in MPS representation on two consecutive tensors written for the selected state.

Hamiltonian of Eq. (5), this effective model must be carefully adapted close to the boundary.

The explicit implementation of $r = 2$ blockade is conceptually very similar, as depicted in Fig. 8. We span the local degrees of freedom over three consecutive atoms and use the quantum state of the two atoms shared by nearest tensors as quantum labels for their common auxiliary leg. The bulk Hamiltonian has the form:

$$h_i = -\frac{\Omega}{2}(\tilde{a}_i\tilde{b}_{i+1}\tilde{c}_{i+2} + \text{H.c.}) - \Delta\tilde{q}_i + V_3\tilde{q}_i\tilde{p}_{i+1}. \tag{A2}$$

In this case, the term $\tilde{a}_i\tilde{b}_{i+1}\tilde{c}_{i+2} + \text{H.c.}$ represents the first term in Eq. (5a) of the main text, which flips an atom between ground and Rydberg states. The only nonzero elements are $\tilde{a}\,|h_1\rangle = |h_2\rangle$, $\tilde{b}\,|h_1\rangle = |h_3\rangle$ and $\tilde{c}\,|h_1\rangle = |h_4\rangle$. The terms $\tilde{q}_i$ and $\tilde{p}_i$ represent the density of the local sites i and $i+2$ correspondingly, with only a single nonzero entree $\tilde{q}\,|h_4\rangle = |h_4\rangle$ and $p_i\,|h_1\rangle = |h_1\rangle$. The interaction $V_3 n_i n_{i+3}$ transforms into

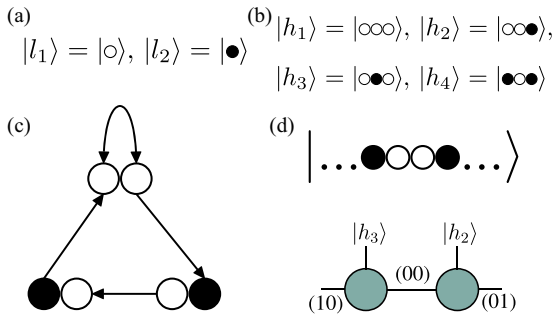

FIG. 8. Mapping of the $r = 2$ blockade model onto a model preserving the block diagonal structure of tensors. (a) Local Hilbert space of the original model $|l_i\rangle$. (b) New local Hilbert space spanned over three consecutive sites. (c) Fusion graph for the recursive construction of the left environment (for the right environment, the direction of arrows should be reverted). (d) Example of the label assignment in MPS representation on two consecutive tensors written for the selected state.

a nearest-neighbor interaction $V_2\tilde{q}_i\tilde{p}_{i+1}$ under the new basis. Similarly to the $r = 1$ case, this Hamiltonian has to be adapted close to the edges to capture the boundary terms.

2. Ground-state calculations

The initial state defined at time $t = 0$ is a ground state at a given point in the phase diagram sufficiently far from the transition. This point is located either in the disordered phase (corresponding to the starting point for the Kibble-Zurek mechanism) or in the ordered period-3 or period-4 phases (the starting points for the backward sweeps for the finite-time scaling of the order parameter).

The ground state was determined with imaginary time-evolving block decimation (TEBD) for the two blockade models. We used second-order Trotter decomposition. Maximal bond dimension was kept at $D = 300$, and singular values below $\chi > 10^{-6}$ were truncated. Convergence criteria were based on the order parameter, with calculations considered converged when the relative variation of the order parameter was smaller than 10^{-9}.

Deep inside the ordered phase, the correlation length is very small, and the energy cost of the domain wall formation is relatively cheap. Therefore, there are many low-lying excited states above the ground states. When the system is close to the classical limit, and the entanglement is low, the TEBD is often stuck at such states with multiple domain walls. To circumvent this issue, we take as a starting guess a classical state (with $D = 1$) that resembles the expected pattern of occupied and empty sites and then perform four sweeps to converge for a given quantum point inside the ordered phase.

3. Simulation of dynamics

Simulations of dynamics in the blockade model were performed using a second-order TEBD. For the $r = 1$ blockade, a two-site Trotterization was applied, while for the $r = 2$ blockade, a three-site Trotterization was used. The time step was maintained at $\delta t = 0.1$, and the maximum bond dimension and singular value cutoff were set to $D = 300$ and $\chi > 10^{-6}$ correspondingly.

Figure 9 shows convergence with respect to bond dimension for Kibble-Zurek(KZ) dynamics across transitions of various types. In Figs. 9(a) and 9(b), we present the extracted density of kinks formed across the three-state Potts and for the Ashkin-Teller point correspondingly as a function of sweep rates for bond dimension ranging from $D = 50$ to $D = 300$. It is clear from the figure that the finite-bond dimension effect is stronger for the Ashkin-Teller point, but in both cases, the results for the two largest bond dimensions are indistinguishable.

Figure 9(c) shows the density of kinks formed while crossing the $p = 3$ chiral transition. Figure 9(d) shows the convergence of the extracted density of kinks for a given sweep rate s as a function of bond dimension D.

APPENDIX B: KINK OPERATORS

Kinks can be counted in two different ways. One way is counting the number of domain walls. Figure 10 depicts the types of domain walls that can appear in period-3 as described

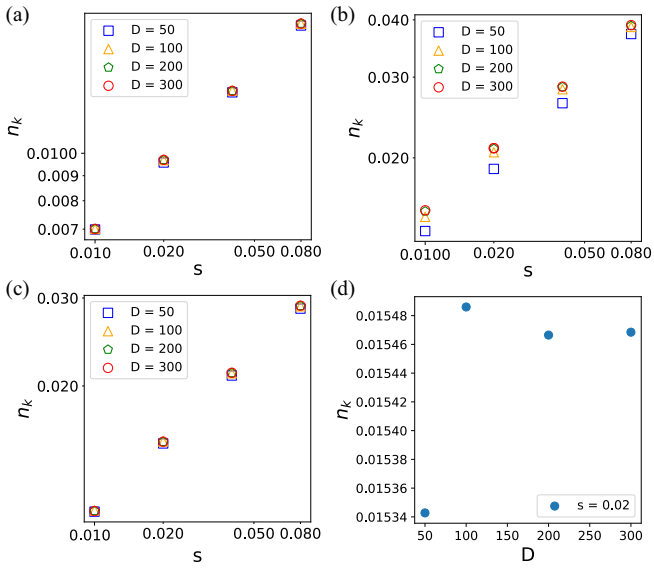

FIG. 9. Density of kinks as a function of sweep rate in a log - log scale for various maximal bond dimensions D measured after crossing (a) the three-state Potts transition, (b) the Ashkin-Teller transition, and (c) the chiral transition. (d) Density of kinks formed across the chiral transition for a given sweep rate as a function of bond dimension D.

in Ref. [9]. An alternative method for counting kinks is using an operator that counts the absence of an ordered state. This *no-order* operator would be (1 − •○○ − ○○• − ○•○) in the period-3 case, and quantifies a kink every time the periodicity of the phase is not followed. These two methods of counting kinks are not always equivalent. For instance, the first method would count one kink in the state •○○••○○•, while the second method would count two kinks. Additionally, the first method would not count any kink in the state •○○○○○•, since the type of domain of the chain does not change, while the second method would count three kinks.

In Fig. 11, we compare the KZ scaling using the two above-mentioned counting methods. Figure 11(a) compares two different cuts through the Potts point for a $r = 1$ blockade, while Fig. 11(b) compares two final distances from the AT point in the $r = 2$ blockade model. In all cases, blue squares

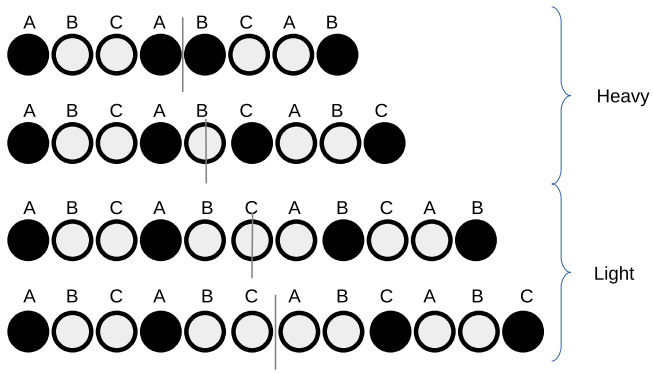

FIG. 10. Types of domain walls in the period 3 phase. There are three types of domains, depending on the label A, B, or C on top of the black dot.

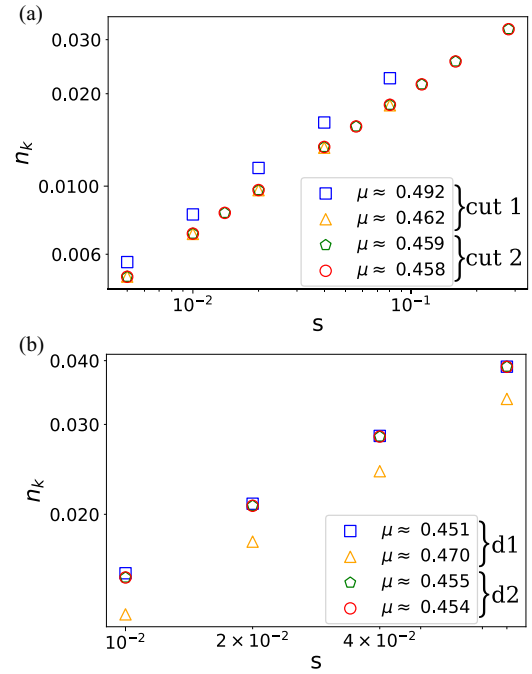

FIG. 11. KZ scaling for the density kinks measured as domain walls (orange triangles and red circles) or with a *no-order* operator (blue squares and green pentagons) for (a) two different cuts through the Potts point for the $r = 1$ blockade model and (b) two final distances from the AT points for the $r = 2$ blockade model.

and green pentagons represent the density of kinks measured with the no-order operator while orange triangles and red circles represent the density of domain walls as described in Fig. 10.

For the $r = 1$ blockade model, data points representing the density of domain walls for the two different cuts and the density kinks using the no-order operator for cut 2 overlap and are close to the theoretical value $\mu = 0.454$. In contrast, data points representing the density of kinks for the no-order operator are off and far from 0.454. However, for $r = 2$ the opposite situation occurs. Data points representing the density of kinks measured with the no-order operator for the two different final distances d1 (short) and d2 (long) and the

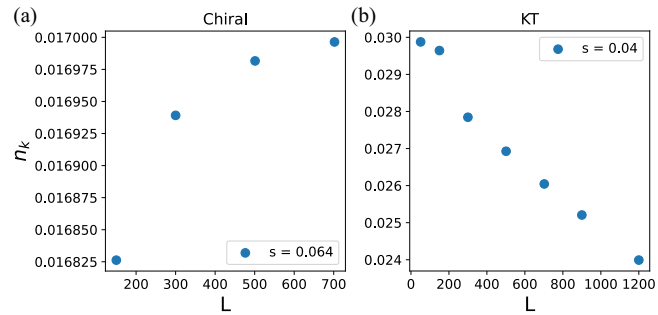

FIG. 12. Finite-size effect of the density of kinks formed by sweeping from the disordered phase to the period-3 phase across (a) the direct chiral transition and (b) the intermediate floating phase separated from the disordered phase by the Kosterlitz-Thouless (KT) transition. The value of sweep rate s is indicated at each panel.

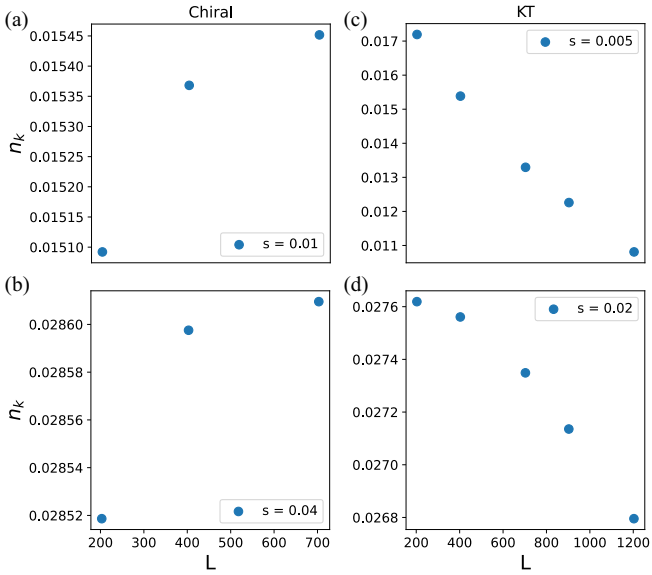

FIG. 13. Finite-size effect of the density of kinks formed by sweeping from the disordered phase to the period-4 phase across (a), (b) the direct chiral transition and (c), (d) the intermediate floating phase separated from a disordered phase by the Kosterlitz-Thouless (KT) transition. The trajectories for panels (a), (b) and for panels (c), (d) are identical.

density of domain walls for d2 overlap and are close to the theoretical value $\mu = 0.44$, while the density of domain walls for d1 is off and far from 0.44. Similar effects were found for different cuts and final distances from the critical point, where convergence always occurred faster for the density of domain walls in the $r = 1$ blockade and for the density of kinks calculated with the no-order operator for the $r = 2$ blockade.

We believe that the discrepancy between the two methods comes from the rare appearance of unlikely events—the state •○○•○○• is forbidden by the blockade, while the state •○○○○• is energetically more costly than any other type of domain walls sketched in Fig. 10. However, sweeping along certain trajectories, for example, those along which incommensurability is nonmonotonous [17,20] the probability of these events might increase. In our research we compared different trajectories, different start and end points and pick ups the kink operators that is the most robust: domain wall operators for period-3 and no-order operator for period-4.

APPENDIX C: FINITE-SIZE EFFECTS IN KIBBLE-ZUREK MECHANISM

In the main text, we argue that in the Kibble-Zurek mechanism, the intermediate floating phase can be distinguished from the direct transition by tracking the finite-size effects in the density of kinks formed by sweeping through the criticality. Figure 12 shows the density of kinks as a function of the system size for the two cuts presented in Fig. 1 of the main text. Figure 12(a) depicts a cut through the chiral transition. Through this cut, the density of kinks increases with the system size L. Figure 12(b) shows the cut through the floating phase, which is mainly governed by the

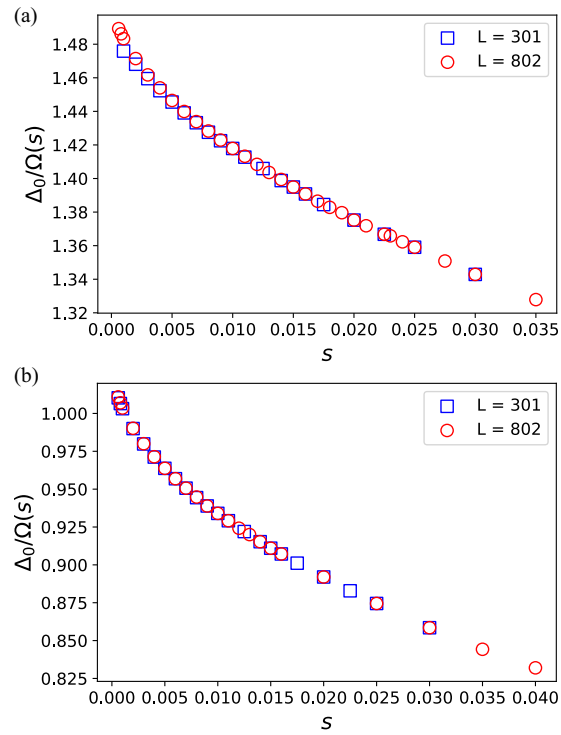

FIG. 14. Comparison of the system size effect in the finite-time scaling for (a) a direct transition and (b) an intermediate floating phase for two different system sizes. In both figures, the difference is visible only for very small sweep rates.

Kosterlitz-Thouless (KT) transition between the disordered and the floating phases. In contrast to the direct transition, the density of kinks systematically decreases with the system size.

The Kibble-Zurek mechanism across the transitions into the period-4 phase with a $r = 2$ blockade model shows qualitatively similar finite-size effects as in the period-3 case. The results for period-4 are summarized in Fig. 13.

APPENDIX D: ORDER PARAMETER

In this Appendix, we define the order parameter associated with the gaped period-3 and period-4 phases with broken translation symmetry. As an order parameter, we use the local amplitude of the local density that we average over the whole finite-size chain. Explicitly, for the period-3 case, we use

$$O = \frac{1}{L-2}\sum_{i=1}^{L-2} \max_i(|n_i - n_{i+1}|, |n_i - n_{i+2}|), \tag{D1}$$

and for the period-4,

$$O = \frac{1}{L-3}\sum_{i=1}^{L-3} \max_i(|n_i - n_{i+1}|, |n_i - n_{i+2}|, |n_i - n_{i+3}|). \tag{D2}$$

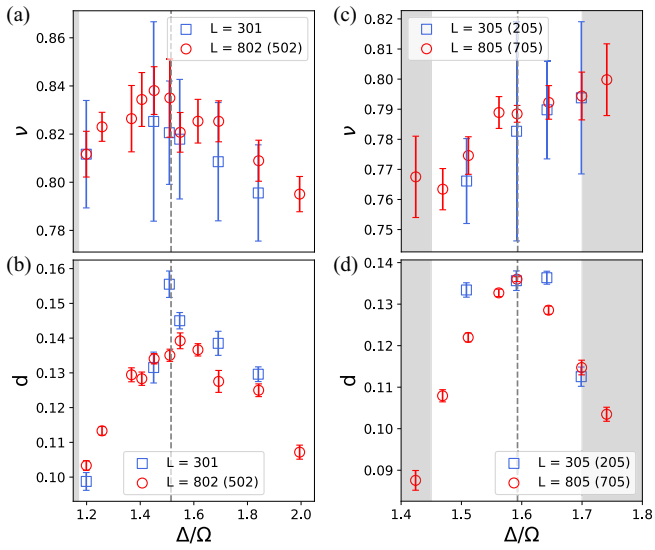

FIG. 15. Correlation length critical exponent ν (a), (c) and scaling dimension of the order parameter $d = \beta/\nu$ (b), (d) extracted by combining the Kibble-Zurek mechanism with finite-time scaling across the transition (a), (b) into period-3 and (c), (d) into period-4 phases.

APPENDIX E: FINITE-SIZE EFFECT IN THE FINITE-TIME SCALING

Figure 14 compares the finite-time scaling (FTS) for two different system sizes. For both system sizes, direct transition [see Fig. 14(a)] and sweep through a floating phase [see Fig. 14(b)], we observe an almost perfect overlap except for the slowest sweep rates.

APPENDIX F: DERIVED CRITICAL EXPONENTS

In this Appendix, we present additional results of the critical exponents that can be derived from the Kibble-Zurek mechanism and the finite-time scaling of the order parameter. In particular, we show the correlation length critical exponent ν across various cuts into the period-3 [see Fig. 15(a)] and into the period-4 [see Fig. 15(c)] phases. In both cases, the critical exponent ν of the chiral transition stays within ≈5–6% of the value at the corresponding conformal point. Our results for the period-3 case [see Fig. 15(a)] agree with the results on the chiral clock model reporting the decrease of ν away from the Potts point [35]. Curiously enough, for the period-4 case, we see that on one side of the transition, ν might increase. It would be interesting to clarify the behavior of ν with a more accurate systematic estimate of ν across the period-4 transition.

In addition, we extract the scaling dimension $d = \beta/\nu$ of the operator that defines the order parameter. These results are summarized in Figs. 15(b) and 15(d).

APPENDIX G: RYDBERG MODEL WITH $1/r^6$ INTERACTION

1. Technical details

For the two-site density matrix renormalization group calculations [5,6], the decaying $1/r^6$ van der Waals interaction was expressed as a sum of 11 exponentials [7,49]; i.e., $1/r^6 = \sum_{i=1}^{11} c_i \lambda_i^r$. The coefficients c_i and exponents λ_i were determined by minimizing the cost function defined as

$$\sum_{r=1}^{L} |\frac{1}{r^6} - \sum_{i=1}^{11} c_i \lambda_i^r|. \tag{G1}$$

This optimization process followed the method described in Ref. [49]. Convergence was declared when variations in the energy per site were $\Delta E < 10^{-8}$.

To match the ordered phase and boundary conditions, the system sizes were chosen in the form $L = Np + 1$, where N is an integer, and p is the periodicity of the ordered phase.

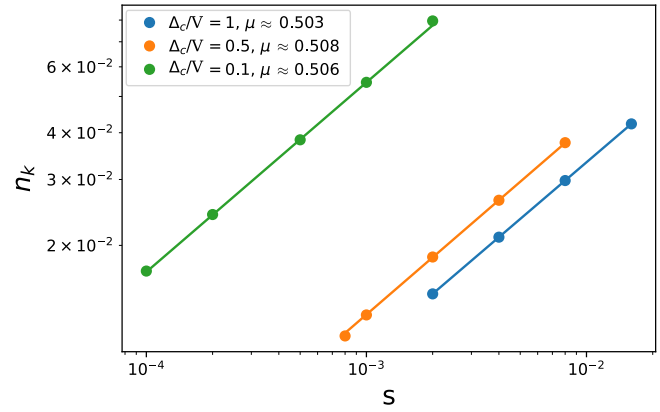

FIG. 16. Scaling of the density of kinks n_k with the sweep rate for a disordered to period $p = 2$ phase transition in the Rydberg model at different critical values of detuning Δ_c. The transition belongs to the Ising universality class characterized by a Kibble-Zurek exponent $\mu = 0.5$. The extracted value of μ is in excellent agreement with theoretical predictions.

2. Simulation of dynamics

For the Rydberg model with $1/r^6$ van der Waals interactions, time evolution was simulated using the time-dependent variational principle (TDVP) [50,51]. The long-range interactions were approximated using a sum of 7 exponentials; the maximum error in this approximation was $\sim 10^{-10}$, with a cost function $\sim 1.3 \times 10^{-19}$. Different δt for various sweep rates and critical points were tested during 24 h simulations. The values of δt that gave the fastest simulations were taken for surrounding sweep rates and critical points. Truncation criteria were maintained at $\chi > 10^{-6}$, and the maximum bond dimension was set to $D = 400$.

3. Ising transition

We benchmark our method with Ising transition [15,24] into period-2 phase for which there are theory predictions for all critical exponents ($\nu = 1$, $z = 1$, $\mu = 0.5$).

Figure 16 shows scaling of the density of kinks and extracted Kibble-Zurek critical exponent μ for three different cuts across the Ising transition—the agreement is always within 2%.

[1] S. Sachdev, Quantum phase transitions, Phys. World **12**, 33 (1999).

[2] T. Giamarchi, *Quantum Physics in One Dimension*, Internat. Ser. Mono. Phys. (Clarendon Press, Oxford, UK, 2004).

[3] P. D. Francesco, P. Mathieu, and D. Sénéchal, *Conformal Field Theory, Graduate Texts in Contemporary Physics* (Springer, New York, NY, 1997).

[4] A. M. Tsvelik, *Quantum Field Theory in Condensed Matter Physics*, 2nd ed. (Cambridge University Press, Cambridge, UK, 2003).

[5] S. R. White, Density matrix formulation for quantum renormalization groups, Phys. Rev. Lett. **69**, 2863 (1992).

[6] S. Östlund and S. Rommer, Thermodynamic limit of density matrix renormalization, Phys. Rev. Lett. **75**, 3537 (1995).

[7] U. Schollwöck, The density-matrix renormalization group in the age of matrix product states, Ann. Phys. **326**, 96 (2011).

[8] S. Paeckel, T. Köhler, A. Swoboda, S. R. Manmana, U. Schollwöck, and C. Hubig, Time-evolution methods for matrix-product states, Ann. Phys. **411**, 167998 (2019).

[9] D. A. Huse and M. E. Fisher, Domain walls and the melting of commensurate surface phases, Phys. Rev. Lett. **49**, 793 (1982).

[10] M. den Nijs, The domain wall theory of two-dimensional commensurate-incommensurate phase transitions, Phase Transitions Crit. Phenom. **12**, 219 (1988).

[11] J. Schreiner, K. Jacobi, and W. Selke, Experimental evidence for chiral melting of the Ge(113) and Si(113) 3×1 surface phases, Phys. Rev. B **49**, 2706 (1994).

[12] D. L. Abernathy, S. Song, K. I. Blum, R. J. Birgeneau, and S. G. J. Mochrie, Chiral melting of the Si(113) (3×1) reconstruction, Phys. Rev. B **49**, 2691 (1994).

[13] W. Selke and J. M. Yeomans, A Monte Carlo study of the asymmetric clock or chiral Potts model in two dimensions, Z. Phys. B **46**, 311 (1982).

[14] D. A. Huse and M. E. Fisher, Commensurate melting, domain walls, and dislocations, Phys. Rev. B **29**, 239 (1984).

[15] A. Keesling, A. Omran, H. Levine, H. Bernien, H. Pichler, S. Choi, R. Samajdar, S. Schwartz, P. Silvi, S. Sachdev *et al.*, Quantum Kibble–Zurek mechanism and critical dynamics on a programmable Rydberg simulator, Nature (London) **568**, 207 (2019).

[16] N. Chepiga and F. Mila, DMRG investigation of constrained models: From quantum dimer and quantum loop ladders to hard-boson and Fibonacci anyon chains, SciPost Phys. **6**, 033 (2019).

[17] N. Chepiga and F. Mila, Floating phase versus chiral transition in a 1D hard-boson model, Phys. Rev. Lett. **122**, 017205 (2019).

[18] I. A. Maceira, N. Chepiga, and F. Mila, Conformal and chiral phase transitions in Rydberg chains, Phys. Rev. Res. **4**, 043102 (2022).

[19] G. Giudici, A. Angelone, G. Magnifico, Z. Zeng, G. Giudice, T. Mendes-Santos, and M. Dalmonte, Diagnosing Potts criticality and two-stage melting in one-dimensional hard-core boson models, Phys. Rev. B **99**, 094434 (2019).

[20] N. Chepiga and F. Mila, Kibble-zurek exponent and chiral transition of the period-4 phase of Rydberg chains, Nat. Commun. **12**, 414 (2021).

[21] S. Whitsitt, R. Samajdar, and S. Sachdev, Quantum field theory for the chiral clock transition in one spatial dimension, Phys. Rev. B **98**, 205118 (2018).

[22] N. Chepiga and F. Mila, Lifshitz point at commensurate melting of chains of Rydberg atoms, Phys. Rev. Res. **3**, 023049 (2021).

[23] R. Samajdar, S. Choi, H. Pichler, M. D. Lukin, and S. Sachdev, Numerical study of the chiral Z3 quantum phase transition in one spatial dimension, Phys. Rev. A **98**, 023614 (2018).

[24] M. Rader and A. M. Läuchli, Floating phases in one-dimensional Rydberg Ising chains, arXiv:1908.02068.

[25] B. E. Lüscher, F. Mila, and N. Chepiga, Critical properties of the quantum Ashkin-Teller chain with chiral perturbations, Phys. Rev. B **108**, 184425 (2023).

[26] P. Fendley, K. Sengupta, and S. Sachdev, Competing density-wave orders in a one-dimensional hard-boson model, Phys. Rev. B **69**, 075106 (2004).

[27] J. M. Kosterlitz and D. J. Thouless, Ordering, metastability and phase transitions in two-dimensional systems, J. Phys. C: Solid State Phys. **6**, 1181 (1973).

[28] V. L. Pokrovsky and A. L. Talapov, Ground state, spectrum, and phase diagram of two-dimensional incommensurate crystals, Phys. Rev. Lett. **42**, 65 (1979).

[29] W. H. Zurek, U. Dorner, and P. Zoller, Dynamics of a quantum phase transition, Phys. Rev. Lett. **95**, 105701 (2005).

[30] J. Dziarmaga, Dynamics of a quantum phase transition: Exact solution of the quantum Ising model, Phys. Rev. Lett. **95**, 245701 (2005).

[31] J. Dziarmaga, Dynamics of a quantum phase transition and relaxation to a steady state, Adv. Phys. **59**, 1063 (2010).

[32] T. W. B. Kibble, Topology of cosmic domains and strings, J. Phys. A: Math. Gen. **9**, 1387 (1976).

[33] W. H. Zurek, Cosmological experiments in superfluid helium? Nature (London) **317**, 505 (1985).

[34] B. Damski, The simplest quantum model supporting the Kibble-Zurek mechanism of topological defect production: Landau-Zener transitions from a new perspective, Phys. Rev. Lett. **95**, 035701 (2005).

[35] R.-Z. Huang and S. Yin, Nonequilibrium critical dynamics in the quantum chiral clock model, Phys. Rev. B **99**, 184104 (2019).

[36] S. Gong, F. Zhong, X. Huang, and S. Fan, Finite-time scaling via linear driving, New J. Phys. **12**, 043036 (2010).

[37] F. Zhong, Finite-time scaling and its applications to continuous phase transitions, in *Applications of Monte Carlo Method in Science and Engineering*, edited by S. Mordechai (IntechOpen, Rijeka, 2011), Chap. 18.

[38] Y. Huang, S. Yin, B. Feng, and F. Zhong, Kibble-Zurek mechanism and finite-time scaling, Phys. Rev. B **90**, 134108 (2014).

[39] J. Dziarmaga and W. H. Zurek, Quench in the 1D Bose-Hubbard model: Topological defects and excitations from the Kosterlitz-Thouless phase transition dynamics, Sci. Rep. **4**, 5950 (2014).

[40] B. Gardas, J. Dziarmaga, and W. H. Zurek, Dynamics of the quantum phase transition in the one-dimensional Bose-Hubbard model: Excitations and correlations induced by a quench, Phys. Rev. B **95**, 104306 (2017).

[41] J. C. Bridgeman, A. O'Brien, S. D. Bartlett, and A. C. Doherty, Multiscale entanglement renormalization ansatz for spin chains with continuously varying criticality, Phys. Rev. B **91**, 165129 (2015).

[42] G. Albertini, B. M. McCoy, J. H. H. Perk, and S. Tang, Excitation spectrum and order parameter for the integrable n-state chiral Potts model, Nucl. Phys. B **314**, 741 (1989).

[43] R. J. Baxter, Superintegrable chiral Potts model: Thermodynamic properties, an "inverse" model, and a simple associated hamiltonian, J. Stat. Phys. **57**, 1 (1989).

[44] J. L. Cardy, Critical exponents of the chiral Potts model from conformal field theory, Nucl. Phys. B **389**, 577 (1993).

[45] J. Zhang, S. H. Cantú, F. Liu, A. Bylinskii, B. Braverman, F. Huber, J. Amato-Grill, A. Lukin, N. Gemelke, A. Keesling *et al.*, Probing quantum floating phases in Rydberg atom arrays, arXiv:2401.08087.

[46] K.-L. Pham, T. F. Gallagher, P. Pillet, S. Lepoutre, and P. Cheinet, Coherent light shift on alkaline-earth Rydberg atoms from isolated core excitation without autoionization, PRX Quantum **3**, 020327 (2022).

[47] N. Chepiga, Tunable quantum criticality in multicomponent Rydberg arrays, Phys. Rev. Lett. **132**, 076505 (2024).

[48] X.-J. Yu, Dynamical phase transition and scaling in the chiral clock Potts chain, Phys. Rev. A **108**, 062215 (2023).

[49] B. Pirvu, V. Murg, J. I. Cirac, and F. Verstraete, Matrix product operator representations, New J. Phys. **12**, 025012 (2010).

[50] J. Haegeman, J. I. Cirac, T. J. Osborne, I. Pižorn, H. Verschelde, and F. Verstraete, Time-dependent variational principle for quantum lattices, Phys. Rev. Lett. **107**, 070601 (2011).

[51] J. Haegeman, C. Lubich, I. Oseledets, B. Vandereycken, and F. Verstraete, Unifying time evolution and optimization with matrix product states, Phys. Rev. B **94**, 165116 (2016).